

ARTICLE

DOI: 10.1038/s41467-017-02454-8

OPEN

# Electrically reversible cracks in an intermetallic film controlled by an electric field

Z.Q. Liu<sup>1</sup>, J.H. Liu<sup>1</sup>, M.D. Biegalski<sup>2</sup>, J.-M. Hu<sup>3</sup>, S.L. Shang<sup>3</sup>, Y. Ji<sup>3</sup>, J.M. Wang<sup>1</sup>, S.L. Hsu<sup>4</sup>, A.T. Wong<sup>5</sup>, M.J. Cordill<sup>6</sup>, B. Gludovatz<sup>7</sup>, C. Marker<sup>3</sup>, H. Yan<sup>1</sup>, Z.X. Feng<sup>1</sup>, L. You<sup>8</sup>, M.W. Lin<sup>2</sup>, T.Z. Ward<sup>5</sup>, Z.K. Liu<sup>3</sup>, C.B. Jiang<sup>1</sup>, L.Q. Chen<sup>3</sup>, R.O. Ritchie<sup>4,9</sup>, H.M. Christen<sup>2</sup> & R. Ramesh<sup>4,9,10</sup>

Cracks in solid-state materials are typically irreversible. Here we report electrically reversible opening and closing of nanoscale cracks in an intermetallic thin film grown on a ferroelectric substrate driven by a small electric field ( $\sim 0.83$  kV/cm). Accordingly, a nonvolatile colossal electroresistance on-off ratio of more than  $10^8$  is measured across the cracks in the intermetallic film at room temperature. Cracks are easily formed with low-frequency voltage cycling and remain stable when the device is operated at high frequency, which offers intriguing potential for next-generation high-frequency memory applications. Moreover, endurance testing demonstrates that the opening and closing of such cracks can reach over  $10^7$  cycles under 10- $\mu$ s pulses, without catastrophic failure of the film.

<sup>1</sup>School of Materials Science and Engineering, Beihang University, Beijing 100191, China. <sup>2</sup>Center for Nanophase Materials Sciences, Oak Ridge National Laboratory, Oak Ridge, TN 37831, USA. <sup>3</sup>Department of Materials Science and Engineering, The Pennsylvania State University, University Park, PA 16802, USA. <sup>4</sup>Department of Materials Science and Engineering, University of California, Berkeley, CA 94720, USA. <sup>5</sup>Materials Science and Technology Division, Oak Ridge National Laboratory, Oak Ridge, TN 37831, USA. <sup>6</sup>Erich Schmid Institute of Materials Science, Austrian Academy of Sciences, and Department of Material Physics, Montanuniversität Leoben, Jahnstr. 12, 8700 Leoben, Austria. <sup>7</sup>School of Mechanical and Manufacturing Engineering, UNSW Sydney, Sydney, NSW 2052, Australia. <sup>8</sup>School of Optical and Electronic Information, Huazhong University of Science and Technology, Wuhan 430074, China. <sup>9</sup>Materials Sciences Division, Lawrence Berkeley National Laboratory, Berkeley, CA 94720, USA. <sup>10</sup>Department of Physics, University of California, Berkeley, CA 94720, USA. Correspondence and requests for materials should be addressed to Z.Q.L. (email: zhiqi@buaa.edu.cn)



Recent efforts on the integration of magnetic intermetallic alloy thin films with functional ferroelectric oxides have created exciting opportunities for manipulating magnetism and resistivity of intermetallics via small electric fields, which offers great promise for low-energy-consuming memory device applications<sup>1–5</sup>. Such heterostructures, such as FeRh/BaTiO<sub>3</sub> and FeRh/0.72PbMg<sub>1/3</sub>Nb<sub>2/3</sub>O<sub>3</sub>–0.28PbTiO<sub>3</sub> (PMN-PT), rely on the strong interfacial-strain-mediated magnetoelectric coupling between the piezoelectric effect in the ferroelectric layer and the phase instability around the phase transition of the FeRh layer to generate giant magnetization and resistivity modulation<sup>1,2,4</sup>.

In addition, the piezoelectric effect of ferroelectric oxides has been extensively employed in mechanical energy harvesting, mechanical sensors, and motors. Nevertheless, the strength degradation of ferroelectric ceramics under cyclic electric fields often generates cracks due to the microscopic internal stress produced at domain boundaries by electrostriction and domain-switching deformations<sup>6–10</sup>, which are detrimental to functionality in most applications. The cracks typically further grow upon cycling of electric fields, thus promoting premature fatigue failures in ferroelectric ceramics. The growth dynamics of cracks in ferroelectric ceramics is indeed closely related to the polarity of the electric field relative to the prepoling field. For example, an opposite electric field relative to the prepoling field enhances the crack propagation, while an electric field of the same polarity inhibits the crack propagation<sup>11</sup>. Also, the occurrence of mechanical opening and closing of cracks under an alternating electric field has been found as the major mechanism for electric-field-induced crack growth in ferroelectric ceramics<sup>12</sup>.

Reversible, reproducible, and durable mechanical sensors based on cracks have been demonstrated although cracks were considered as defects to be avoided<sup>13</sup>. More importantly, the crack formation in solid-state materials could be well controlled by bending<sup>13</sup>, notches, and confined surface stress<sup>14–16</sup>. In this work, we demonstrate a new type of heterostructures consisting of intermetallic alloys and ferroelectric oxides for room-temperature memory applications; interestingly, we can utilize precisely the otherwise problematic existence of cracks to create a functional device. Instead of utilizing electronic phase transitions of intermetallic alloys and the piezoelectric effect of ferroelectric oxides, here we propose to employ the mechanical properties of intermetallic alloys and the opening/closing of cracks induced by cyclic electric fields in ferroelectric oxides. By integrating moderately ductile intermetallic alloy thin films onto ferroelectric oxide single-crystal substrates, mechanical opening and closing of cracks in ferroelectric oxides driven by external electric fields can be transferred into the intermetallic films via interfacial strain mediation, and then, the ferroelectric oxides effectively act to mechanically open and close fissures in the intermetallic films in a similar fashion to opening/closing an electrical breaker, but here, at the nanoscale, consequently resulting in a colossal on–off ratio of the resistance switching across cracks in the intermetallic thin films.

## Results

**Materials and sample growth.** Intermetallic alloys are a unique class of materials consisting of ordered alloy compounds formed between two or more metallic elements, where different elements occupy specific sites in the crystal lattice. Their mechanical properties are intermediate between metals, which are generally soft and ductile, and ceramics, which are generally hard and brittle. Strikingly, the properties of intermetallics can be strongly influenced by small changes in the system, for example, small variations in the microstructure can result in large changes in strength and ductility<sup>17</sup>.

To utilize the opening and closing of cracks in ferroelectric ceramics as electrically detectable switches, intermetallic thin films are ideal candidates to be integrated on top because of their intermediate mechanical properties and resistivity. That is because with a metal thin film grown on a ferroelectric substrate, when cracks form and open in the ferroelectric oxide with application of a cyclic electric field, corresponding cracks in the metal thin film may well not form immediately, or at all, due to the good ductility of the metal layer. Conversely, if a ceramic film is grown on top of a ferroelectric oxide crystal, when the cracks in ferroelectric substrate close, the cracks in the ceramic film may not be fully closed and remain partially open, leading to a high resistance across the crack, making this system highly insulating and prone to premature failure as ceramic materials tend to be extremely brittle. Therefore, intermetallic alloys are precisely the right materials to be considered for such a structure.

MnPt, an antiferromagnetic (AFM) intermetallic alloy, forms a CuAu-I (*L*<sub>10</sub>)-type tetragonal crystal structure with *a* = 2.827 Å and *c* = 3.669 Å. The tetragonal phase is stable with Pt composition between 33 and 60 at%<sup>18</sup>, where the lattice constants and the Néel temperature strongly depend on the Pt composition. Our theoretical calculations on the elastic properties of the AFM Mn<sub>50</sub>Pt<sub>50</sub> reveal that its bulk modulus *B* = 177.3 GPa (Supplementary Note 1) is close to the measured elastic modulus of MnPt films (Supplementary Note 2), shear modulus *G* = 96.5 GPa, and Young's modulus *E* = 245.1 GPa. This yields a bulk/shear modular ratio *B/G* ≈ 1.84, indicating that MnPt is likely to be brittle due to the AFM Mn atoms according to Pugh's criterion<sup>19</sup> (Supplementary Note 3). Thus, defect-free MnPt is expected to be very close to the empirical boundary between ductile and brittle. Indeed, our previous electrical measurements demonstrate that MnPt thin films are metallic with room-temperature resistivity  $\rho \sim 10^{-4} \Omega \text{ cm}^5$ . In light of this, we conclude that MnPt represents a possibly ideal candidate material to develop a crack-based memory device in an intermetallic/ferroelectric heterostructure, where the ferroelectric layer effectively acts to mechanically open and close fissures in the MnPt layer to act as the nanoscale analog of a conventional switch.

To realize such a switch, we deposited MnPt thin films onto (001)-oriented PMN-PT single-crystal substrates (5 × 5 × 0.3 mm<sup>3</sup>), which were coated with Au on the backside and prepoled by applying a positive bias to the backside Au before deposition. Figure 1 shows a cross-section TEM image of a MnPt/PMN-PT heterostructure. The MnPt layer is polycrystalline with multiple

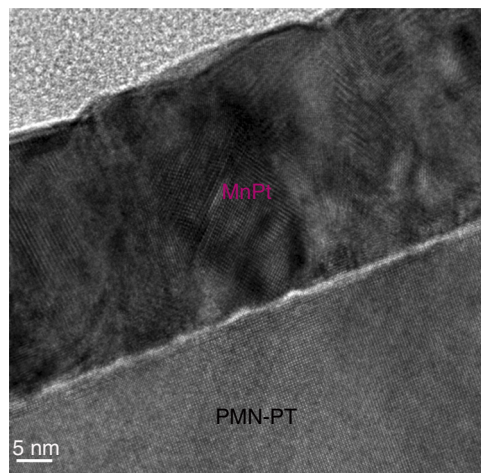


**Fig. 1** Structural characterization. Cross-section transmission electron microscopy of a 35-nm-thick MnPt/PMN-PT heterostructure. The scale bar on the left bottom corresponds to 5 nm



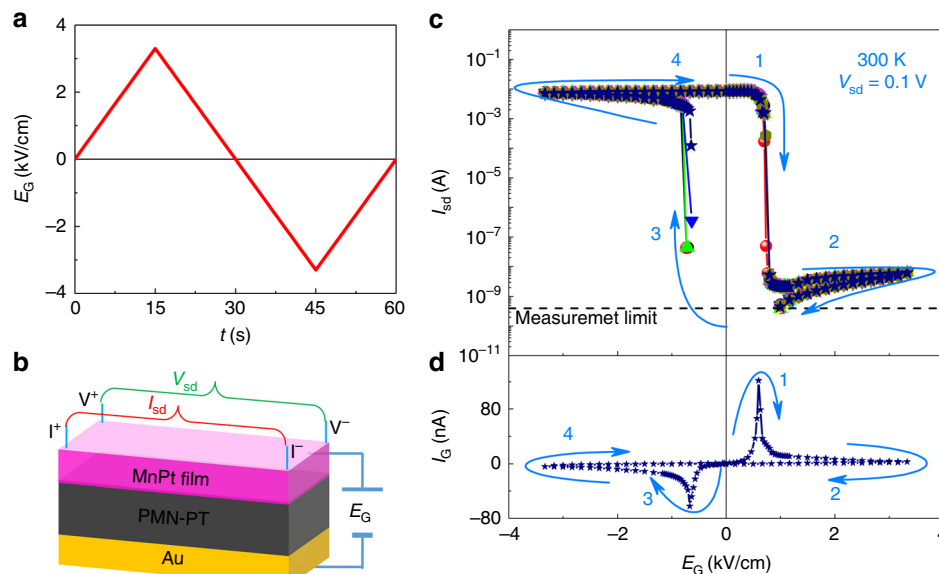


**Fig. 2** Colossal electrical switching at room temperature. **a** Electrical waveform for creating cracks in PMN-PT. **b** Schematic of the resistance measurement geometry. **c** Repeated and reproducible switching of the channel current  $I_{sd}$  as a function of the gate electric field  $E_G$ , measured by  $V_{sd} = 0.1$  V at 300 K. The data for nine continuous cyclic field loops are plotted (data connecting segments 2 and 3 are not shown because they are below the measurement limit). **d** Corresponding switching current in the PMN-PT substrate of the last scan. The arrows and numbers in **c** and **d** are the guidance of the field-sweep sequence

orientations. Moreover, the interface is reasonably sharp, with an interface layer that is only  $\sim 1$ -nm thick. Scanning transmission electron microscopy–energy-dispersive spectroscopy (STEM–EDS) analysis revealed that the chemical composition of the MnPt film was  $Mn_{44.2}Pt_{55.8}$  ( $\pm 2$  at%). The Mn deficiency may be because the lighter Mn atoms are more strongly scattered to higher angles by the background Ar atoms.

**Colossal electroresistance.** To generate cracks in the PMN-PT substrate which would then propagate through the MnPt film as well, a triangular cyclic electric field, with an amplitude of 3.3 kV/cm and a period of 60 s (Fig. 2a), was applied between the top MnPt film and the back Au electrode. After 100 cycles, electric-field-driven reversible opening and closing of cracks with sub-micrometer width and few micrometers length were visible under a microscope. The opening of the cracks occurs when the applied field is opposite to the prepoling field direction, while closure sets in when the external field is reversed. It is important to remind ourselves that ferroelectric crystals do not switch uniformly but rather through the motion of domain walls, which are partially pinned at surface defects. The local strains occurring near a surface are therefore highly nonuniform, and not symmetric with respect to the reversal of the applied field. In our case, this leads to a switching behavior such that a positive bias (segments 1 and 2) results in crack opening, whereas a negative bias (segments 3 and 4) leads to the closing of the cracks, despite the fact that the average strain state of the crystal in both directions is such that one would expect a compressive state—locally, however, domain motion clearly leads to a tensile behavior without which the cracks would not open. Because the metal layer is deposited onto a surface with preexisting domains and pinning defects, these two states are highly reproducible and not symmetric with a field, contrary to the macroscopic strain in the crystal.

Subsequent electrical measurements were performed to examine the effect of the crack opening and closing on the resistance of the top MnPt film. To probe the macroscopic response of an ensemble of cracks, the Van der Pauw geometry was utilized in the initial measurements, which is schematically

represented in Fig. 2b. At  $E_G = 0$  kV/cm, a fixed voltage of  $V_{sd} = 0.1$  V induces a current of  $I_{sd} \sim 10^{-2}$  A, corresponding to a room-temperature resistance of  $\sim 10$   $\Omega$  (Fig. 2c). Increasing  $E_G$  to +0.83 kV/cm drives a sudden drop in  $I_{sd}$  over several orders of magnitude to  $\sim 10^{-9}$  A. Accordingly, the switching current in the PMN-PT exhibits a sharp peak (Fig. 2d), characteristic of the ferroelectric domain switching.  $I_{sd}$  continues to decrease with increasing  $E_G$ , and becomes too low to read as we approach  $E_G$  to +1 kV/cm. Subsequent reduction of  $E_G$  to 0 kV/cm does not change the open state of the measurement circuit, illustrating a nonvolatile high-resistance state.

$I_{sd}$  increases and can be experimentally resolved again as  $E_G$  decreases to  $-0.83$  kV/cm. The corresponding peak in the leakage current of PMN-PT shows the opposite domain switching relative to that at +0.83 kV/cm. Above this gate charge,  $I_{sd}$  rapidly increases to  $\sim 10^{-2}$  A and saturates. The saturation current remains as the gate bias is removed at  $E_G = 0$  kV/cm. This provides a nonvolatile low-resistance state. Finally, we note that the writing and reading signals are applied independently of each other, and reading of the device cannot trigger a back-switching behavior.

**Mechanism for the reversible cracks.** To directly visualize the status of cracks for nonvolatile high- and low-resistance states, atomic force microscopy was utilized to image a MnPt thin-film surface as  $E_G$  was cycled from +3.3 kV/cm to 0 kV/cm and from  $-3.3$  kV/cm to 0 kV/cm. As seen in Fig. 3a, a crack is open with a gap width of  $\sim 250$  nm after sweeping  $E_G$  from +3.3 kV/cm to 0, corresponding to the high-resistance open state in the resistance measurements. Conversely, the crack closes after the heterostructure experiences a negative  $E_G$  of  $-3.3$  kV/cm, yielding an electrically intact low-resistance state (Fig. 3b). The depth of the crack is much larger than the thin-film thickness of 35 nm, which is consistent with our interpretation that the cracks are transferred from the ferroelectric oxide into the thin film via interfacial strain. Moreover, the clear correspondence between the resistance switching and the leakage current peaks in Fig. 2 demonstrates that the opening and closing of the cracks in PMN-PT are



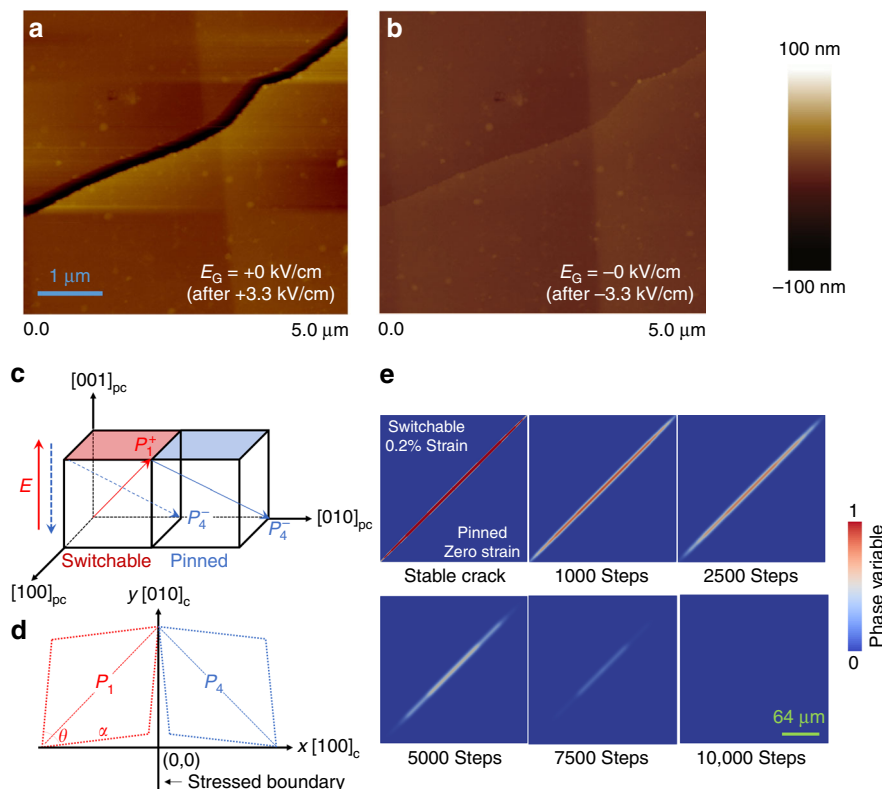


**Fig. 3** Reversible crack driven by an electric field. Atomic force microscopy images ( $5 \times 5\ \mu\text{m}^2$ ) of a single crack in the MnPt film after scanning the gate electric field  $E_G$  **a** from  $+3.3$  kV/cm to  $0$  kV/cm and **b** from  $-3.3$  kV/cm to  $0$  kV/cm. **c, d** Schematics showing that electric-field ( $E$ )-induced reversible and nonvolatile crack formation and closure on the (001) PMN-PT surface can result from a reversible and nonvolatile  $E$ -induced  $109^\circ$  polarization switching. A two-domain configuration consisting of one switchable polarization domain and one pinned domain is considered. Such reversible  $109^\circ$  polarization switching can repeatedly induce an in-plane shear strain of about  $0.2\%$  in the switchable domain, which will repeatedly stress the domain boundary. The  $0.2\%$  strain is calculated based on the lattice parameters ( $a, \theta$ ) of the rhombohedral (001) PMN-PT. **e** Phase-field simulations of the crack evolution when the strain is ON (the first image in the first row) and OFF (the remaining images). Color bar shows the magnitude of the phase variable, which equals  $1$  in the crack region and  $0$  in the PMN-PT, and changes continuously across their interface

induced by internal stresses generated at domain boundaries due to domain-switching deformations.

Figure 3c–d shows one possible mechanism for the electric-field-induced crack formation and closure on the surface of PMN-PT. A simplified two-domain configuration is considered, where one polarization domain (left) can be switched by an electric field while the other is pinned (Fig. 3c). In this case, an upward electric-field ( $E$ )-induced  $109^\circ$  polarization switching from  $P_4^-$  to  $P_1^+$  at the surface of (001) PMN-PT crystal (demonstrated by experiments<sup>20</sup>) can cause a local shear strain of about  $0.2\%$  in the left domain. This  $0.2\%$  shear strain is calculated based on the lattice parameters of the rhombohedral PMN-PT at  $300\ \text{K}$ <sup>21</sup> ( $a = 4.017\ \text{\AA}$ ,  $\theta = 89.89^\circ$ , see Fig. 3d). Such a large strain will cause severe increase in the elastic energy such that a crack forms along the wall to relax the stress, at the expense of producing additional surface energy. Once the  $P_1^+$  domain is switched back to the  $P_4^-$  domain by applying a downward electric field, the strain returns to zero. The crack will then close to reduce surface energy. Since the  $E$ -induced  $109^\circ$  polarization switching has been experimentally demonstrated to be both reversible and nonvolatile<sup>20</sup>, the associated crack opening and closing should also be reversible and nonvolatile. Overall, the electric-field-induced crack formation and closure are mainly governed by the competing electromechanical-strain-related elastic energy and the surface energy. The higher the surface energy, the harder the crack formation (i.e., the higher the crack formation energy).

A simplified phase-field model was developed (see “Methods” section) to demonstrate this mechanism. As shown in Fig. 3e, the

crack can remain stable when a  $0.2\%$  strain is applied to the top half of the simulation zone (corresponding to the  $P_1^+$  domain), while the strain in the other half (corresponding to the  $P_4^-$  domain) is set as zero. Once the strain in the entire zone is set as zero (corresponding to a uniform  $P_4^-$  domain), the crack will gradually vanish to reduce the surface energy (see the corresponding dynamic evolution process in Fig. 3e).

**High-frequency properties and endurance test.** Given that cracks in a ferroelectric are known to have the potential to result in macroscopic fracture, we further investigate the crack growth dynamics of MnPt/PMN-PT heterostructures under cyclic electric fields. The samples were first excited by 100 cycles of triangular waveform to create cracks. The samples were then mounted into a setup that is similar to what was used in ref. <sup>12</sup>, but is capable of measuring smaller samples to monitor the cracking progress operando. As plotted in Fig. 4a, the crack growth as a function of the cycling frequency demonstrates that excitation frequencies above  $300\ \text{Hz}$  can significantly suppress crack propagation and can withstand a much longer cycling process. The origin of the exponential dependence of the crack lifetime on frequency is not very clear and is still under investigation.

To understand the reason for which cracks grow more slowly at high frequency, we performed measurements using short pulses. It was found that the reversible opening and closing of the cracks can be driven by gate electric pulses as short as  $10\ \mu\text{s}$  spaced by  $30\ \text{ms}$ . We therefore performed the endurance test for a single crack ( $\sim 300$ -nm width,  $\sim 100$ - $\mu\text{m}$  length) via two-probe



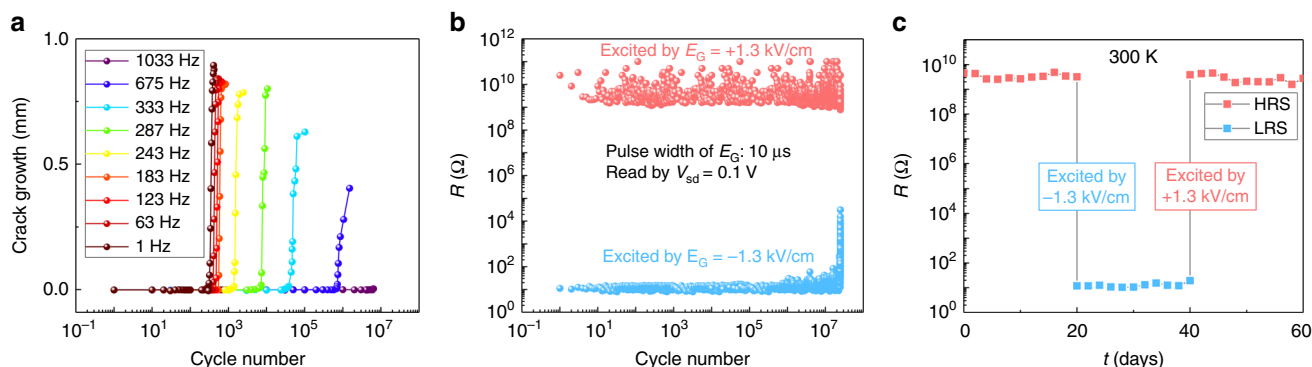


**Fig. 4** Crack growth dynamics and endurance testing. **a** Crack growth length vs. electric cycling number under different cyclic field frequencies. The amplitude of the cyclic electric field with triangular waveform is 1.3 kV/cm. **b** Two-probe resistance measured by 0.1 V vs. gate electric field pulse number across a single crack. The pulses are of 10- $\mu$ s width and the amplitude is 1.3 kV/cm. **c** Retention of different resistance states of a single crack up to 60 days

resistance measurements. Upon applying  $\pm 1.3$  kV/cm and 10- $\mu$ s electric pulses to the PMN-PT substrate, the resistance across the crack was measured by a small voltage of 0.1 V. The reversible opening and closing of the crack can be cycled more than  $10^7$  times before the crack grows rapidly and the closing state degrades (Fig. 4b), which is good for memory applications<sup>22</sup>. This shows that the different behavior at different frequencies is largely related to the amount of time the device is subject to the field around the switching moments, which provides us with flexibility in designing devices for use in different circumstances.

**Memory performance.** Based on our experience on small device fabrication of such heterostructures, the crack state is stable for at least 22 months. Representative data for the retention of the high-resistance and low-resistance states (HRS and LRS) collected in 2 months are shown in Fig. 4c. The excellent nonvolatility is consistent with crack formation as a consequence of the local strain and deformation at domain boundaries induced by non-uniform domain switching. In contrast, the macroscopic strain in PMN-PT has a symmetric butterfly loop and is volatile at zero field<sup>23</sup>. These results demonstrate a prototype memory device based on an intermetallic/ferroelectric heterostructure. It is expected that both the switching speed<sup>24</sup> and the cycling number could be largely increased by patterning the cracks into much smaller scales or further refining the device layout.

## Discussion

Compared with the intrinsic resistivity modulation of intermetallic alloys by piezoelectric strain in intermetallic/ferroelectric heterostructures, such as FeRh/PMN-PT<sup>2</sup> and FeRh-BaTiO<sub>3</sub> (Ref. 4), where the  $\rho$ - $E_G$  curves are almost symmetric with “butterfly” shape, the resistance switching in crack-based intermetallic/ferroelectric heterostructures exhibits “square” loops (Fig. 2c). This is a favorable attribute for nonvolatile information storage. Both types of resistance switching predominantly rely on the domain switching of ferroelectrics, and therefore, the switching speed should be intrinsically comparable. However, the former can only be operated around the phase transition temperatures of the intermetallic alloys, and the resistance modulation is limited to the intrinsic resistivity difference between different electronic phases, which, for example, is maximally  $\sim 50\%$  for FeRh<sup>25</sup> between the ferromagnetic and AFM phases. In contrast, crack-based switching can be operated over a large temperature range below ferroelectric  $T_c$  and is capable of a colossal resistance on-off ratio.

The microstructure and composition of an intermetallic alloy are important for its mechanical properties, such as ductility. Compared with the defect-free Mn<sub>50</sub>Pt<sub>50</sub> in our initial theoretical

calculations, the practical films are polycrystalline and have a chemical ratio of Mn<sub>44.2</sub>Pt<sub>55.8</sub>, which could thus possess a different ductility than theoretically predicted. Although more detailed studies on the mechanical properties of such thin films are needed, the fact that the MnPt/PMN-PT heterostructures exhibit remarkably reversible on and off states suggests that the polycrystalline feature and the current composition of the MnPt films may be important for achieving the excellent closure state with “healed” electrical conductivity.

Such intermetallic/ferroelectric heterostructures are indeed also microelectromechanical systems (MEMS). The crack formation is expected to occur even in 1- $\mu$ m-thick high-quality PMN-PT films<sup>26</sup>, which would lead to an operation voltage of  $\sim 0.1$  V. In contrast, most of conventional MEMS need an operation voltage of 3–8 V for pulling in counter electrodes<sup>27</sup>. Compared with conventional MEMS that consist of multiple layers and need complicated fabrication processes, the one-layer structure of our devices is much simpler and the fabrication process is much easier. In addition, most of conventional MEMS are volatile at zero voltage while our devices are nonvolatile.

The elastic energy for switching the polarization in ferroelectric oxides can be estimated as  $E_{\text{switching}} = 1/2 P_s V S$ <sup>28</sup>, where  $P_s$  is the saturation ferroelectric polarization ( $\sim 25$   $\mu\text{C}/\text{cm}^2$  for PMN-PT),  $V$  is the switching voltage, and  $S$  is the cell area. Such an energy consumption is predominant for opening and closing the cracks when such a device is of large size. However, as the device is scaled down, the bonding energy of the freshly created surfaces of a crack could be dominant, which can be estimated as the surface energy times the interface area of the crack. For example, if a crack device can be scaled down to a footprint area of  $100 \times 100$  nm<sup>2</sup> with PMN-PT thickness of 1  $\mu\text{m}$  for integrated device applications, the energy consumption for switching the polarization would be  $E_{\text{switching}} = 1/2 P_s V S = 12.5$   $\mu\text{C}/\text{cm}^2 \times 0.83$  kV/cm  $\times 1$   $\mu\text{m} \times 100$  nm  $\times 100$  nm  $\approx 0.1$  fJ. In contrast, considering a typical surface energy value of  $\sim 1$  J/m<sup>2</sup>, a film thickness of 35 nm, such as that in our case, and a crack length of 100 nm, the surface energy of the two surfaces of the crack is  $2 \times 1$  J/m<sup>2</sup>  $\times 35 \times 10^{-9}$  m  $\times 100 \times 10^{-9}$  m = 7 fJ, which is much larger than the polarization-switching energy.

In summary, instead of trying to avoid the cracks in ferroelectrics that have been regarded as being highly detrimental in terms of promoting premature fatigue failures, we have utilized cyclic-field-induced cracks in ferroelectric oxides by integrating moderately ductile intermetallic alloy films on top and realized electrically controllable switches with a colossal on-off electro-resistance ratio. Together with the high-frequency properties and the excellent endurance performance, this work illustrates a prototype crack-based memory device. Such an approach could



be feasible for a wide range of intermetallic/ferroelectric heterostructures, thus opening a new avenue to information storage.

## Methods

**Sample growth.** MnPt thin films were sputtered from a Mn<sub>50</sub>Pt<sub>50</sub> target onto (001)-oriented PMN-PT single-crystal substrates ( $5 \times 5 \times 0.3 \text{ mm}^3$ ) in a radio frequency sputtering system with a base pressure of  $3 \times 10^{-7}$  Torr. All the PMN-PT substrates were coated with Au on the backside and prepoled by applying a positive bias to the backside Au before deposition. To avoid interfacial oxidation of MnPt and chemical reaction between MnPt and PMN-PT, the deposition temperature was kept at 375 °C. The sputtering power and Ar gas pressure were 40 W and 3 mTorr, respectively. To avoid possible breaking of the PMN-PT substrates during variations in temperature, the ramp rate was kept at 5 °C/min for both heating and cooling. The deposition rate was 0.19 Å/s, as determined by transmission electron microscopy (TEM) measurements. With a deposition time of 30 min, the resulting thin-film thickness of the MnPt was ~35 nm.

**Electrical and structural and mechanical measurements.** Electrical contacts onto MnPt films were made by Al wires via wire bonding. The electrical measurements were performed by Keithley 2400 source meters at room temperature. For the STEM characterization, cross-sectional wedged samples were prepared by mechanical polishing on Allied High Tech Multiprep and ion milled by a Gatan Precision Ion Milling System. By utilizing an electron probe to scan thin films to achieve high resolution of local regions, Z-contrast scanning transmission electron microscope images were acquired by high-angle annular detector on FEI TitanX microscope at 300 kV. For mechanical crack growth measurements, the samples were immersed in silicon oil inside a transparent plexiglass container and subjected to a cyclic electric field through the bolts attached to the electrodes. The crack growth was monitored and measured by a microscopy system and a digit charge-coupled device system. Pulse measurements for cycling endurance testing were performed by an Agilent pulse generator.

**Calculation methods.** The single-crystal elastic constants of MnPt were predicted by the strain–stress method based on first-principles calculations<sup>29</sup>, and the elastic properties for polycrystalline MnPt were estimated using the Hill approach<sup>30</sup> (see Supplementary Methods for details).

**Phase-field simulations.** We introduce a continuous phase variable  $\eta$  to describe the crack region ( $\eta = 1$ ), the bulk PMN-PT ( $\eta = 0$ ), and their interface (more precisely, the surface of the PMN-PT, where  $0 < \eta < 1$ ). In the framework of diffuse-interface theory, the total free energy  $F_{\text{tot}}$  of such a two-phase system can be written as:

$$F_{\text{tot}}(\eta, \epsilon) = \int_V \left[ f_{\text{chem}}(\eta) + \frac{\kappa_{ij}}{2} \nabla_i \eta \nabla_j \eta + f_{\text{elast}}(\eta, \epsilon) \right] dV, \quad (1)$$

where  $\kappa_{ij}$  is the gradient energy coefficient (J/m) that is proportional to both the surface energy  $\gamma$  and the surface depth (or interface thickness) of the PMN-PT. As there are no available data on the surface energy of the complex perovskite 0.72PMN–0.28PT, we used the surface energy of (001) BaTiO<sub>3</sub> ( $\approx 1.076 \text{ J/m}^2$  in ref. <sup>31</sup>), a prototypical ferroelectric oxide with perovskite structure, as an approximation. To describe the crack region and the PMN-PT, the chemical free energy density  $f_{\text{chem}}$  takes a function that has two global energy minima at  $\eta = 0$  and 1,

$$f_{\text{chem}}(\eta) = w\eta^2(1 - \eta)^2, \quad (2)$$

where  $w$  is the potential barrier separating the two energy minima, and is proportional to the ratio of surface energy to the surface depth<sup>32</sup>. The elastic energy density  $f_{\text{elast}}$  is calculated as:

$$f_{\text{elast}}(\eta, \epsilon) = \frac{1}{2} \sigma_{ij} \epsilon_{ij} = \frac{1}{2} c_{ijkl}(\eta) \epsilon_{kl} \epsilon_{ij} = \frac{1}{2} c_{ijkl}(\eta) (\bar{\epsilon}_{kl} + \delta \epsilon_{kl} - \epsilon_{kl}^0) (\bar{\epsilon}_{ij} + \delta \epsilon_{ij} - \epsilon_{ij}^0), \quad (3)$$

where the spatially variant elastic stiffness tensor  $c_{ijkl}(\eta)$  is given by

$$c_{ijkl}(\eta) = c_{ijkl}^{\text{PMN-PT}}(1 - h(\eta)) + c_{ijkl}^{\text{crack}} h(\eta). \quad (4)$$

Here, the use of the interpolating function  $h(\eta) = \eta^3(6\eta^2 - 15\eta + 10)$  makes  $c_{ijkl}^{\text{PMN-PT}}$  when  $\eta = 0$ ;  $c_{ijkl}^{\text{crack}}$  when  $\eta = 1$ ;  $c_{ijkl}$  is a combination of  $c_{ijkl}^{\text{PMN-PT}}$  and  $c_{ijkl}^{\text{crack}}$  at the solid–crack interface. The elastic stiffness tensor of PMN-PT  $c_{ijkl}^{\text{PMN-PT}}$  is taken from ref. <sup>33</sup>, while the  $c_{ijkl}^{\text{crack}}$  is set  $10^{11}$  times smaller than the  $c_{ijkl}^{\text{PMN-PT}}$  (not exactly zero to avoid numerical issues).

The  $\bar{\epsilon}_{kl}$ ,  $\delta \epsilon_{kl}$ , and the  $\epsilon_{kl}^0$  in Eq. (3) represent the homogeneous strain, heterogeneous strain, and the stress-free strain, respectively. The homogeneous strain  $\bar{\epsilon}_{kl}$  describes the average deformation of the system. It is therefore spatially invariant and is zero in the present system. The stress-free strain  $\epsilon_{kl}^0$  describes the influence of the local polarization on the local strain in a ferroelectric material, and

is given by

$$\epsilon_{kl}^0 = Q_{klmn} P_m P_n, \quad (5)$$

where  $Q_{klmn}$  is the electrostrictive stiffness tensor;  $P_m$  and  $P_n$  represent local polarization vectors. In the two-domain configuration (Fig. 3c),  $\epsilon_{12}^0$  is set as 0.2% in the  $P_1^+$  domain and 0 in the  $P_1^-$  domain (see “Discussion” section in main text). The heterogeneous strain  $\delta \epsilon_{kl}$  is given by

$$\delta \epsilon_{kl} = \frac{1}{2} \left( \frac{\partial u_k}{\partial x_l} + \frac{\partial u_l}{\partial x_k} \right), \quad (6)$$

where the spatially variant  $u$  is the local mechanical displacement in the system, and is obtained by solving the mechanical equilibrium equation  $\partial \sigma_{ij} / \partial x_j = 0$ , expanded as

$$c_{ijkl} \frac{\partial^2 u_k}{\partial x_l \partial x_j} = c_{ijkl} \frac{\partial \epsilon_{kl}^0}{\partial x_j}. \quad (7)$$

Equation (7) is numerically solved using a Fourier-spectral iterative perturbation method<sup>34</sup>.

The evolution of the crack is modeled using relaxational kinetics<sup>35,36</sup>

$$\frac{\partial}{\partial t} = -LH(f_{\text{elast}} - f_c) \frac{\delta F_{\text{tot}}}{\delta}, \quad (8)$$

where  $L$  is the mobility of the crack–solid interface, which was set as a constant for simplicity<sup>35,36</sup>.  $H(f_{\text{elast}} - f_c)$  is the Heaviside step function that equals 0 when  $f_{\text{elast}} < f_c$  and when  $f_{\text{elast}} \geq f_c$ . Here, the  $f_c$  is a parameter for modeling the nucleation and growth of the crack, which can be related to the surface energy through the Griffith relation<sup>36</sup>. Since the surface energy is proportional to the crack formation energy,  $f_c$  can be related to the crack formation energy. Indeed, in our present model, the value of  $f_c$  ( $\approx 10 \text{ MJ/m}^3$ ) is found to be dependent on the surface energy we chose. The variational derivative  $\delta F_{\text{tot}} / \delta$  represents the thermodynamic driving force for the evolution of the phase variable  $\eta$ , expanded as

$$\frac{\delta F_{\text{tot}}}{\delta} = \frac{\partial(f_{\text{chem}} + f_{\text{elast}})}{\partial} - \kappa_{ij} \nabla_i \nabla_j. \quad (9)$$

Equation (8) is then solved using a numerically efficient semi-implicit Fourier-spectral method<sup>36</sup> in a 3D discretional grid system of  $256\Delta x \times 256\Delta y \times 2\Delta z$ , with  $\Delta x = \Delta y = \Delta z = 1 \mu\text{m}$ . The obtained spatial distribution of  $\eta$  at different time steps (Fig. 3e) describes the evolution of the crack morphology.

**Data availability.** The data and simulation codes that support the findings of this study are available from the corresponding author on request.

Received: 10 March 2017 Accepted: 3 December 2017

Published online: 03 January 2018

## References

- Cherifi, R. O. et al. Electric-field control of magnetic order above room temperature. *Nat. Mater.* **13**, 345–351 (2014).
- Lee, Y. et al. Large resistivity modulation in mixed-phase metallic systems. *Nat. Commun.* **6**, 5959 (2015).
- Phillips, L. C. et al. Local electrical control of magnetic order and orientation by ferroelastic domain arrangements just above room temperature. *Sci. Rep.* **5**, 10026 (2015).
- Liu, Z. Q. et al. Full electroresistance modulation in a mixed-phase metallic alloy. *Phys. Rev. Lett.* **116**, 097203 (2016).
- Liu, Z. Q. et al. Epitaxial growth of intermetallic MnPt films on oxides and large exchange bias. *Adv. Mater.* **28**, 118–123 (2016).
- Makino, H. & Kamiya, N. Effects of dc electric field on magnetic properties of piezoelectric ceramics. *Jpn. J. Appl. Phys.* **33**, 5323–5327 (1994).
- Yang, W. & Suo, Z. Cracking in ceramic actuators caused by electrostriction. *J. Mech. Phys. Solids* **42**, 649–663 (1994).
- Lynch, C. S. et al. Electric field induced cracking in ferroelectric ceramics. *Ferroelectrics* **166**, 11–30 (1995).
- Wang, H. Y. & Singh, R. N. Electric field effects on the crack propagation in an electrostrictive PMN-PT ceramic. *Ferroelectrics* **168**, 281–291 (1995).
- Xu, Z. et al. *In situ* transmission electron microscopy study of electric-field-induced microcracking in single crystal Pb(Mg<sub>1/3</sub>Nb<sub>2/3</sub>)O<sub>3</sub>-PbTiO<sub>3</sub>. *Appl. Phys. Lett.* **76**, 3732–3734 (2000).
- Wang, H. Y. & Singh, R. N. Crack propagation in piezoelectric ceramics: effects of applied electric fields. *J. Appl. Phys.* **81**, 7471–7479 (1997).
- Fang, D. N., Zhang, H. Y. & Mao, G. Z. Electric-field-induced fatigue crack growth in ferroelectric ceramics. *Theor. Appl. Fract. Mech.* **54**, 98–104 (2010).



13. Kang, D. et al. Ultrasensitive mechanical crack-based sensor inspired by the spider sensory system. *Nature* **516**, 222–226 (2014).
14. Nam, K. H., Park, I. H. & Ko, S. H. Patterning by controlled cracking. *Nature* **485**, 221–224 (2012).
15. Kim, B. C. et al. Guided fracture of films on soft substrates to create micro/nano-feature arrays with controlled periodicity. *Sci. Rep.* **3**, 3027 (2013).
16. Vandeparre, H., Liu, Q., Mineev, I. R., Suo, Z. & Lacour, S. P. Localization of folds and cracks in thin metal films coated on flexible elastomer foams. *Adv. Mater.* **25**, 3117–3121 (2013).
17. Westbrook, J. H. *Intermetallic Compounds*. (John Wiley and Sons, Inc., New York, 1967).
18. Krén, E. et al. Magnetic structures and exchange interactions in the Mn–Pt system. *Phys. Rev.* **171**, 574–585 (1968).
19. Pugh, S. F. XCII. Relations between the elastic moduli and the plastic properties of polycrystalline pure metals. *Philos. Mag.* **45**, 823–843 (1954).
20. Zhang, S. et al. Electric-field control of nonvolatile magnetization in  $\text{Co}_{40}\text{Fe}_{40}\text{B}_{20}/\text{Pb}(\text{Mg}_{1/3}\text{Nb}_{2/3})_{0.7}\text{Ti}_{0.3}\text{O}_3$  structure at room temperature. *Phys. Rev. Lett.* **108**, 137203 (2012).
21. Noheda, B., Cox, D. E., Shirane, G., Gao, J. & Ye, Z. G. Phase diagram of the ferroelectric relaxor  $(1-x)\text{PbMg}_{1/3}\text{Nb}_{2/3}\text{O}_3$ - $x\text{PbTiO}_3$ . *Phys. Rev. B* **66**, 054104 (2002).
22. Yang, J. J., Strukov, D. B. & Stewart, D. R. Memristive devices for computing. *Nat. Nano* **8**, 13–24 (2013).
23. Thiele, C. et al. Influence of strain on the magnetization and magnetoelectric effect in  $\text{La}_{0.7}\text{A}_{0.3}\text{MnO}_3/\text{PMN-PT}$  (001) ( $A = \text{Sr}, \text{Ca}$ ). *Phys. Rev. B* **75**, 054408 (2007).
24. Li, J. et al. Ultrafast polarization switching in thin-film ferroelectrics. *Appl. Phys. Lett.* **84**, 1174–1176 (2004).
25. Suzuki, I. et al. Clear correspondence between magnetoresistance and magnetization of epitaxially grown ordered FeRh thin films. *J. Appl. Phys.* **109**, 07C717 (2011).
26. Baek, S. H. et al. Giant piezoelectricity on Si for hyperactive MEMS. *Science* **334**, 958–961 (2011).
27. Gaddi, R. et al. MEMS technology integrated in the CMOS back end. *Microelectron. Reliab.* **50**, 1593–1598 (2010).
28. Hu, J.-M., Li, Z., Chen, L.-Q. & Nan, C.-W. High-density magnetoresistive random access memory operating at ultralow voltage at room temperature. *Nat. Commun.* **2**, 553 (2011).
29. Shang, S. L., Wang, Y. & Liu, Z. K. First-principles elastic constants of  $\alpha$ - and  $\theta$ - $\text{Al}_2\text{O}_3$ . *Appl. Phys. Lett.* **90**, 101909 (2007).
30. Hill, R. The elastic behaviour of a crystalline aggregate. *Proc. Phys. Soc. A* **65**, 349–354 (1952).
31. Eglitis, R. I. & Vanderbilt, D. Ab initio calculations of  $\text{BaTiO}_3$  and  $\text{PbTiO}_3$  (001) and (011) surface structures. *Phys. Rev. B* **76**, 155439 (2007).
32. Hu, J.-M. et al. Phase-field based multiscale modeling of heterogeneous solid electrolytes: applications to nanoporous  $\text{Li}_3\text{PS}_4$ . *ACS Appl. Mater. Interfaces* **9**, 33341–33350 (2017).
33. Sun, E. & Cao, W. Relaxor-based ferroelectric single crystals: growth, domain engineering, characterization and applications. *Prog. Mater. Sci.* **65**, 124–210 (2014).
34. Hu, S. Y. & Chen, L. Q. A phase-field model for evolving microstructures with strong elastic inhomogeneity. *Acta Mater.* **49**, 1879–1890 (2001).
35. Karma, A., Kessler, D. A. & Levine, H. Phase-field model of mode III dynamic fracture. *Phys. Rev. Lett.* **87**, 045501 (2001).
36. Biner, S. & Hu, S. Y. Simulation of damage evolution in composites: a phase-field model. *Acta Mater.* **57**, 2088–2097 (2009).

## Acknowledgements

Z.Q.L. acknowledges financial support from the National Natural Science Foundation of China (NSFC Grant No. 51771009) and the start-up grant from Beihang University. This work was partially supported by the Laboratory Directed Research and Development (LDRD) Programs of ORNL managed by UT-Battelle, LLC (sample growth) and the DOE Office of Science, Basic Energy Sciences, and Materials Sciences (partial electrical transport). B.G. and R.O.R. were supported by the U.S. Department of Energy, Office of Science, Basic Energy Sciences, Materials Sciences, and Engineering Division. J.-M.H., Y.Ji, and L.-Q.C. acknowledge financial support from the US National Science Foundation under the DMREF program with grant number DMR1629270. R.R. acknowledges financial support from the NSF (Nanosystems Engineering Research Center for Translational Applications of Nanoscale Multiferroic Systems, Cooperative Agreement Award EEC-1160504). We acknowledge Y. Lee for collecting the AFM data. We dedicate this work to the late Dr Michael D. Biegalski, who was not only a well-respected research colleague, but also a wonderful father and husband, a driven athlete, and a dear friend to all of us.

## Author contributions

Z.Q.L. performed sample growth and electrical measurements with assistance from M.D.B., A.T.W., M.W.L., T.Z.W., J.H.L., J.M.W., H.Y., Z.X.F., L.Y. and J.C.B. S.L.H. performed TEM measurements. M.C., B.G. and R.O.R. contributed to mechanical testing of MnPt films. S.L.S., C.M. and Z.K.L. performed theoretical calculations on elastic properties of MnPt. J.-M.H., Y.J. and L.-Q.C. contributed to understanding the mechanism and the phase-field simulations of strain-mediated electric-field-driven crack formation and closure. This project was coordinated by Z.Q.L., H.M.C. and R.R. All authors contributed to the discussion of results. Z.Q.L. wrote the manuscript with help from all other authors.

## Additional information

**Supplementary Information** accompanies this paper at <https://doi.org/10.1038/s41467-017-02454-8>.

**Competing interests:** The authors declare no competing financial interests.

**Reprints and permission** information is available online at <http://npg.nature.com/reprintsandpermissions/>

**Publisher's note:** Springer Nature remains neutral with regard to jurisdictional claims in published maps and institutional affiliations.



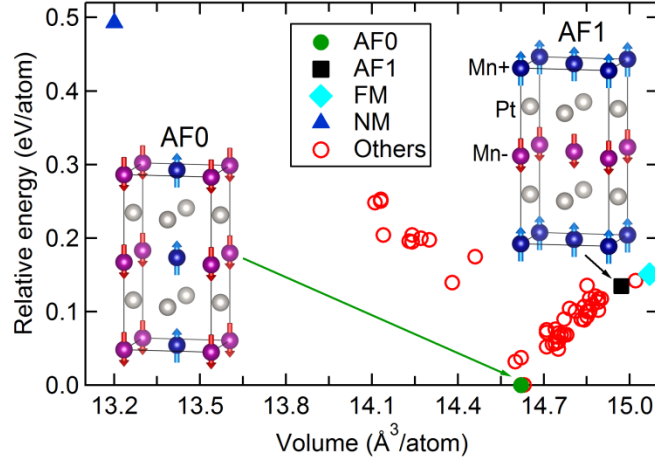
**Open Access** This article is licensed under a Creative Commons Attribution 4.0 International License, which permits use, sharing, adaptation, distribution and reproduction in any medium or format, as long as you give appropriate credit to the original author(s) and the source, provide a link to the Creative Commons license, and indicate if changes were made. The images or other third party material in this article are included in the article's Creative Commons license, unless indicated otherwise in a credit line to the material. If material is not included in the article's Creative Commons license and your intended use is not permitted by statutory regulation or exceeds the permitted use, you will need to obtain permission directly from the copyright holder. To view a copy of this license, visit <http://creativecommons.org/licenses/by/4.0/>.

© The Author(s) 2017



## Supplementary Note 1

**First-principles calculations of MnPt by VASP code.** Starting from a 4-atom  $L1_0$  structure of MnPt (*i.e.*,  $Mn_2Pt_2$ ), we assume that the Mn site can be occupied by either the spin up or the spin down Mn atoms ( $Mn^+$  or  $Mn^-$ ). We tested all the possible 4-, 8-, and 12-atom supercells. Figure S1 shows the relative energy as a function of equilibrium volume of MnPt for these tests.



**Supplementary Figure 1| Relative energy as a function of equilibrium volume of MnPt.** AF, FM and NM stand for antiferromagnetic, ferromagnetic and nonmagnetic structures, respectively.

The present first-principles calculations indicate that:

1. The AF0 is the lowest energy structure (Fig. S1), while the NM is the highest energy structure.
2. Among all the AF structures, the lower energy structure should be the one with the maximum entropy distribution<sup>1</sup> within the Mn sublattice, *i.e.*, the nearest Mn atoms of  $Mn^+$  is  $Mn^-$ , and the nearest Mn atoms of  $Mn^-$  is  $Mn^+$  (see AF0 and AF1).
3. If all the Mn atoms in MnPt structure possess larger magnetic moments ( $> 3.0 \mu_B$ ), then these structures have higher equilibrium volumes with respect to that of AF0. We call these structures the group 1 structures. For the group 1 structures, the FM has the highest (or higher) energy.
4. If one or more Mn atoms in MnPt have smaller magnetic moments ( $< 1.0 \mu_B$ ), then these structures possess lower equilibrium volumes (with respect to AF0), we call these structure as the group 2 structures. Specially, the NM is a structure with the magnetic moment of zero for all Mn atoms.
5. In principle, group 1 structures have lower energies than those of the group 2 structures, indicating that the MnPt phase shows an anti-Invar behavior at high temperatures due to magnetism.
6. The defects of Mn atoms in Mn site (Mn sublattice) will cause a great increase of energy, *i.e.*, the anti-site of spin up Mn ( $Mn^+$ ) and spin down Mn ( $Mn^-$ ). For example, the energy of AF1 (see Fig. S1, due to anti-site of  $Mn^+$  and  $Mn^-$  within the Mn sublattice) is comparable with that of the FM structure. Hence, the defects within Mn sublattice due to



site change of Mn<sup>+</sup> and Mn<sup>-</sup> will cause the more stability of the FM with respect to the AF structure.

7. We also tested other defects, such as Mn vacancy, Pt vacancy, and anti-site of Mn and Pt. These defects will decrease the energy difference between the AF0 phase and the FM phase, but, a significant decrease of their energy difference will be the Mn defects (such as anti-site of Mn<sup>+</sup> and Mn<sup>-</sup>) within the Mn sublattice as shown in Fig. S1.

The calculated structural, elastic and magnetic parameters for the three different magnetic structures are shown in Tabs. S1-S3.

**Supplementary Table 1| Calculated mechanical and magnetic parameters.** Equilibrium properties of three structures from the 4-parameter Birch-Murnaghan equation of state (EOS) fitting<sup>2</sup> after first-principles calculations.

Structure	Volume (Å <sup>3</sup> /atom)	Relative energy (eV/atom)	Bulk modulus (GPa)	B' (the first derivate of bulk modulus with respect to pressure)	Magnetic moment of Mn ( $\mu_B$ /atom)
AF0	14.68	0.000	174.8	5.08	3.7
AF1	15.06	0.132	157.4	4.53	3.8
FM	15.17	0.147	164.0	3.97	3.8

**Supplementary Table 2| Calculated elastic constants.** Single-crystal elastic properties ( $C_{ij}$ ) of AF0 and FM MnPt (unit is GPa) calculated by the strain-stress method according to first-principles calculations<sup>3</sup>.

Structure	$C_{11}$	$C_{12}$	$C_{13}$	$C_{33}$	$C_{44}$	$C_{66}$
AF0	264	115	140	283	123	117
FM	244	108	149	232	99	87
FM <sup>a</sup>	257	89	149	224	100	71

<sup>a</sup> Prediction according to Materials Project database<sup>4</sup>.

**Supplementary Table 3| Calculated bulk modulus, shear modulus, and Young's modulus.** Aggregative elastic properties of MnPt from the  $C_{ij}$  values in Tab. S2, where the Hill approach<sup>5</sup> was employed. These properties include bulk modulus ( $B$ ), shear modulus ( $G$ ), Young's modulus, and Poisson ratio ( $\nu$ ). Note bulk moduli from equation of state (EOS) fitting are 174.8 and 164.0 GPa for AF0 and FM, respectively, which is slightly smaller than the ones from the  $C_{ij}$  values due to more relaxations in EOS fitting<sup>2</sup>.

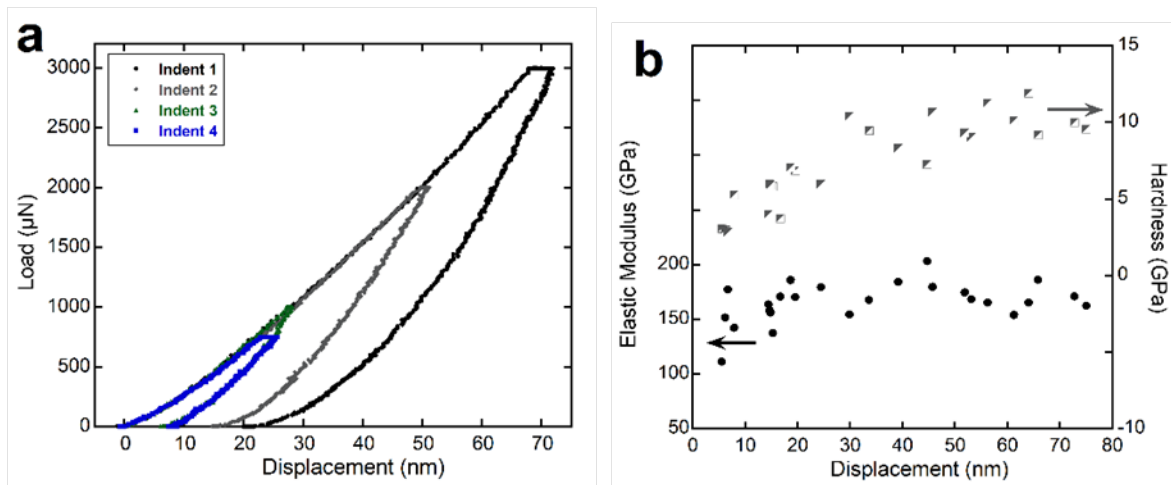
Structure	$B_H$ (GPa)	$G_H$ (GPa)	$E_H$ (GPa)	$B/G$	$\nu$
AF0	177.3	96.5	245.1	1.84	0.27
FM	169.8	72.8	191.2	2.33	0.31
FM <sup>a</sup>	167.6	71.5	187.8	2.34	0.31



<sup>a</sup> Prediction from the Materials Project database<sup>4</sup>.

## Supplementary Note 2

**Mechanical tests of MnPt films.** In order to assess the mechanical behavior of MnPt films, nanoindentation was utilized. A three-sided pyramidal Berkovich tip with a radius of about 100 nm was used to indent the surface of a 35 nm thick MnPt film on a silicon substrate on a Hysitron TriboScope (Minneapolis, MN, USA). Thirty indents were performed within a maximum displacement range between 5-80 nm (Fig. S2a). The representative load-displacement curves illustrate permanent plastic deformation and no pop-ins that would indicate thin film fracture events. From the initial unloading slopes of the load-displacement curves the elastic modulus using the Oliver-Pharr method<sup>6</sup> was calculated as well as the hardness (Fig. S2b). The mechanical properties of the MnPt film should be taken near the surface (5-30 nm) to avoid influence from the substrate. The elastic modulus of the MnPt film was measured to be approximately 155-160 GPa (close to the calculated bulk modulus  $B = 177$  GPa) and the hardness was 5 GPa. A significant increase in the hardness after 30 nm of displacement is an indication of the substrate influence on the measured value.



**Supplementary Figure 2| Nanoindentation results.** **a**, Representative load-displacement curves made using a Berkovich tip illustrating permanent plastic deformation into the MnPt film on silicon. **b**, Calculated elastic modulus and hardness of the MnPt film in the indented displacement range.

## Supplementary Note 3

**Pugh's criterion ( $B/G$  ratio) to judge brittleness/ductility.** The Pugh's criterion based on the  $B/G$  ratio is a simple model to judge the brittleness or ductility of a solid material, since the bulk modulus  $B$  can be considered as the resistance to fracture and the shear modulus  $G$  the resistance to plastic deformation. A critical  $B/G$  ratio (around 1.75) to separate the brittle and ductile materials was implied by Pugh<sup>7</sup> based on *fcc* metals with high melting point. The microscopic origin of this empirical parameter ( $B/G = 1.75$ ) can be understood from an isotropic cubic crystal with Cauchy relations  $C_{11} = 3C_{12}$  and  $C_{12} = C_{44}$ , resulting in a  $B/G$  value of 1.67<sup>8</sup>. The critical value ( $B/G = 1.75$ ) has been widely used in first-principles community for various materials, see such as the work done by Ravindran *et al.*<sup>8</sup> in 1998 for the orthorhombic  $\text{TiS}_2$  by considering the ductile Ti ( $B/G = 2.47$ ) and the brittle Si ( $B/G = 1.49$ ).



Although the criterial  $B/G$  ratio (1.75) was driven from *fcc* metals with high melting point, we found it works for  $L1_0$ -type compounds by considering the brittle TiAl<sup>9</sup> with  $B/G = 1.64$  and the ductile CoPt<sup>10</sup> with  $B/G = 2.00$  (data from the Materials Project database<sup>4</sup>, see Tab. S4). It is worth mentioning that the criterial  $B/G = 1.75$  don't work for all materials as pointed by, for example, Pugh<sup>7</sup>, Gandhi and Ashby<sup>11</sup>.

The present MnPt with  $B/G = 1.84$  should be near-brittle within the category of  $L1_0$ -type compounds, and MnPt is more brittle than its constituent elements, *i.e.*, the metastable *fcc* Mn with  $B/G = 2.14$  and *fcc* Pt with  $B/G = 4.98$ , see Tab. S4. It is further noticed that the brittleness of MnPt stems from the antiferromagnetic Mn atoms by considering the  $B/G$  ratios for the FM and AF MnPt (2.32 vs. 1.84, see Tab. S4).

**Supplementary Table 4| Calculated bulk modulus  $B$  and shear modulus  $G$  as well as the  $B/G$  ratio in the Hill approach.** These elastic properties were taken from the Materials Project database<sup>4</sup> and the present work. All the available  $L1_0$ -type compounds (space group  $P4/mmm$ ) with elastic properties together with the *fcc* Mn and *fcc* Pt are listed.

Formula	Materials Project ID	Space group	$B$ (GPa)	$G$ (GPa)	$B/G$	Note
MnAl	mp-771	$P4/mmm$	133	84	1.58	
TiGa	mp-2767	$P4/mmm$	115	72	1.60	
TiAl	mp-1953	$P4/mmm$	115	70	1.64	Brittle <sup>6</sup>
CoPt	mp-949	$P4/mmm$	216	108	2.00	Ductile <sup>7</sup>
FeNi	mp-2213	$P4/mmm$	187	92	2.03	
FePt	mp-2260	$P4/mmm$	201	92	2.18	
ZnNi	mp-429	$P4/mmm$	146	63	2.32	
MnPt <sup>a</sup>	mp-1670	$P4/mmm$	168	72	2.33	
MnPt <sup>a</sup>		$P4/mmm$	170	73	2.32	This work
MnPt <sup>b</sup>		$P4/mmm$	177	96	1.84	This work
NiPt	mp-945	$P4/mmm$	213	91	2.34	
NbIr	mp-1359	$P4/mmm$	259	105	2.47	
ZnPd	mp-1652	$P4/mmm$	139	55	2.53	
CdPd	mp-1696	$P4/mmm$	110	42	2.62	
MnPd	mp-238	$P4/mmm$	134	51	2.63	
MgIn	mp-2313	$P4/mmm$	40	15	2.67	
ZnPt	mp-894	$P4/mmm$	172	63	2.73	
NbRh	mp-1963	$P4/mmm$	220	79	2.78	
TiIr	mp-1235	$P4/mmm$	228	81	2.81	
CdPt	mp-1194	$P4/mmm$	137	48	2.85	
HgPd	mp-2685	$P4/mmm$	115	35	3.29	
TaRu	mp-1601	$P4/mmm$	252	73	3.45	
TiRh	mp-2583	$P4/mmm$	190	49	3.88	
ZrHg	mp-2510	$P4/mmm$	102	24	4.25	
NbRu	mp-432	$P4/mmm$	237	53	4.47	



CuAu	mp-522	$P4/mmm$	135	28	4.82	
<i>fcc</i> Mn	mp-8634	$Fm\bar{3}m$	280	131	2.14	
<i>fcc</i> Pt	mp-126	$Fm\bar{3}m$	244	49	4.98	

## Supplementary Methods

**First-principles calculations.** In the present work, all density functional theory (DFT) based first-principles calculations were performed by VASP code<sup>12</sup> with the electron-ion interaction described by the projector augmented wave method<sup>13</sup> and the exchange-correlation functional described by the generalized gradient approximation<sup>14</sup>. The  $L1_0$ -type low energy antiferromagnetic (AFM) and the ferromagnetic (FM) structures were employed for MnPt, see details reported previously<sup>15</sup>. Single crystal elastic constants of AFM and FM MnPt were calculated by an efficient strain-stress method<sup>3</sup> with the employed non-zero strains of  $\pm 0.01$ . The same VASP settings as used previously<sup>15</sup>, 5,000 (or 8,000)  $k$ -points per reciprocal atom and plane wave energy cutoff of 270 eV (or 337 eV) were used for structural relaxations (or final static calculations) to calculate elastic constants using VASP. Note that the final static calculations were performed by the tetrahedron method with Blöchl correction<sup>16</sup> for accurate stress results.

In addition, the mentioned energy vs. volume equation of state (EOS) fittings were performed by a 4-parameter Birch-Murnaghan equation<sup>2</sup> in terms of about eight energy vs. volume first-principles data points for each structure. Based on the obtained single crystal elastic constants, aggregative elastic properties were estimated using the Hill approach<sup>5</sup>, including bulk modulus ( $B$ ), shear modulus ( $G$ ), Young's modulus, and Poisson ratio ( $\nu$ ).

## Supplementary References:

1. Shang, S., Wang, Y., Wang, W. Y., Fang, H. & Liu, Z.-K. Low energy structures of lithium-ion battery materials  $\text{Li}(\text{Mn}_x\text{Ni}_x\text{Co}_{1-2x})\text{O}_2$  revealed by first-principles calculations. *Appl. Phys. Lett.* **103**, 53903 (2013).
2. Shang, S. L., Wang, Y., Kim, D. & Liu, Z. K. First-principles thermodynamics from phonon and Debye model: Application to Ni and  $\text{Ni}_3\text{Al}$ . *Comput. Mater. Sci.* **47**, 1040–1048 (2010).
3. Shang, S. L., Wang, Y. & Liu, Z. K. First-principles elastic constants of  $\alpha$ - and  $\theta$ - $\text{Al}_2\text{O}_3$ . *Appl. Phys. Lett.* **90**, 101909 (2007).
4. Jain, A. *et al.* Commentary: The Materials Project: A materials genome approach to accelerating materials innovation. *APL Mater.* **1**, 11002 (2013).
5. Hill, R. The elastic behaviour of a crystalline aggregate. *Proc. Phys. Soc. Sect. A* **65**, 349–354 (1952).
6. Oliver, W. C. & Pharr, G. M. An improved technique for determining hardness and elastic modulus using load and displacement sensing indentation experiments. *J. Mater. Res.* **7**, 1564–1583 (1992).



7. Pugh, S. F. XCII. Relations between the elastic moduli and the plastic properties of polycrystalline pure metals. *Philos. Mag.* **45**, 823–843 (1954).
8. Ravindran, P. *et al.* Density functional theory for calculation of elastic properties of orthorhombic crystals: Application to TiSi<sub>2</sub>. *J. Appl. Phys.* **84**, 4891–4904 (1998).
9. Booth, A. S. & Roberts, S. G. The brittle-ductile transition in  $\gamma$ -TiAl single crystals. *Acta Mater.* **45**, 1045–1053 (1997).
10. Greenberg, B. A. *et al.* Optimised mechanical properties of ordered noble metal alloys. *Platin. Met. Rev.* **47**, 46–58 (2003).
11. Gandhi, C. & Ashby, M. F. Fracture mechanism maps for materials which cleave: F.C.C., B.C.C. and H.C.P. metals and ceramics. *Acta Metall.* **27**, 1565–1602 (1979).
12. Kresse, G. & Furthmüller, J. Efficiency of ab-initio total energy calculations for metals and semiconductors using a plane-wave basis set. *Comput. Mater. Sci.* **6**, 15–50 (1996).
13. Kresse, G. & Joubert, D. From ultrasoft pseudopotentials to the projector augmented-wave method. *Phys. Rev. B* **59**, 1758–1775 (1999).
14. Perdew, J. P., Burke, K. & Ernzerhof, M. Generalized gradient approximation made simple. *Phys. Rev. Lett.* **77**, 3865–3868 (1996).
15. Liu, Z. *et al.* Epitaxial growth of intermetallic MnPt Films on oxides and large exchange bias. *Adv. Mater.* **28**, 118–123 (2016).
16. Blöchl, P. E., Jepsen, O. & Andersen, O. K. Improved tetrahedron method for Brillouin-zone integrations. *Phys. Rev. B* **49**, 16223–16233 (1994).